

# Bright Chromenylum Polymethine Dyes Enable Fast, Four-Color *In Vivo* Imaging with Shortwave Infrared Detection

Emily D. Cosco, Bernardo A. Arús, Anthony L. Spearman, Timothy L. Atallah, Irene Lim, Olivia S. Leland, Justin R. Caram, Thomas S. Bischof, Oliver T. Bruns,\* and Ellen M. Sletten\*



Cite This: *J. Am. Chem. Soc.* 2021, 143, 6836–6846



Read Online

ACCESS |



Metrics & More

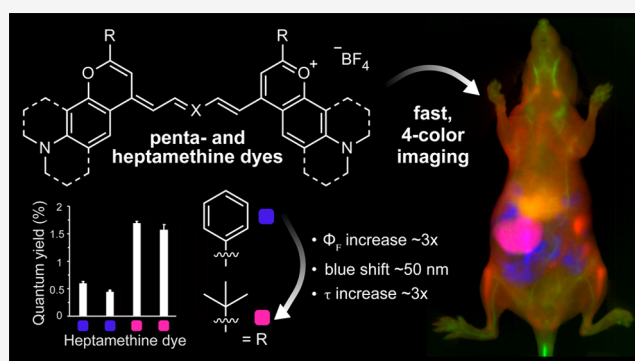


Article Recommendations



Supporting Information

**ABSTRACT:** Optical imaging within the shortwave infrared (SWIR, 1000–2000 nm) region of the electromagnetic spectrum has enabled high-resolution and high-contrast imaging in mice, non-invasively. Polymethine dyes, with their narrow absorption spectra and high absorption coefficients, are optimal probes for fast and multiplexed SWIR imaging. Here, we expand upon the multiplexing capabilities in SWIR imaging by obtaining brighter polymethine dyes with varied excitation wavelengths spaced throughout the near-infrared (700–1000 nm) region. Building on the flavylum polymethine dye scaffold, we explored derivatives with functional group substitution at the 2-position, deemed chromenylum polymethine dyes. The reported dyes have reduced nonradiative rates and enhanced emissive properties, enabling non-invasive imaging in mice in a single color at 300 fps and in three colors at 100 fps. Combined with polymethine dyes containing a red-shifted julolidine flavylum heterocycle and indocyanine green, distinct channels with well-separated excitation wavelengths provide non-invasive video-rate *in vivo* imaging in four colors.



## INTRODUCTION

Optical detection in the shortwave infrared (SWIR, 1000–2000 nm) region of the electromagnetic spectrum furnishes high-sensitivity and high-resolution imaging in small animals. The enhanced performance arises from lower scattering coefficients, reduced tissue autofluorescence, and water absorption improving the contrast in the SWIR compared with the near-infrared (NIR, 700–1000 nm) and visible (VIS, 350–700 nm) regions.<sup>1–4</sup> Since the initial report of SWIR detection for deep-tissue optical imaging in 2009,<sup>5</sup> diverse emitters for this region, including carbon nanotubes,<sup>6</sup> quantum dots,<sup>7,8</sup> rare-earth containing nanoparticles,<sup>9,10</sup> and small molecules,<sup>11,12</sup> have been optimized. These efforts have enabled improvements in imaging speed, up to ~100 fps,<sup>10,13</sup> and the translation of advanced imaging techniques, such as multicolor imaging,<sup>13–15</sup> confocal microscopy,<sup>16,17</sup> and light-sheet microscopy,<sup>18</sup> to this long wavelength region. Further, clinical applications of SWIR detection have been studied in human subjects.<sup>19,20</sup>

Recent efforts in multiplexing *in vivo* using non-invasive modalities such as bioluminescence,<sup>21</sup> magnetic resonance,<sup>22</sup> and photoacoustic<sup>23</sup> imaging have paved the way to study multiple biological parameters simultaneously. We recently reported a strategy for multiplexed non-invasive optical imaging in mice, namely, excitation multiplexing with single-channel SWIR detection.<sup>13</sup> This approach hinges on SWIR-emissive fluorescent probes with well-spaced absorption spectra that can

be preferentially excited with orthogonal wavelengths of light (Figure 1a) and detected in the SWIR (Figure 1b) in tandem on the millisecond time scale. An additional benefit of the excitation multiplexing approach is that similar contrast and resolution in all channels is achieved by maintaining the same SWIR detection window. In the initial report, non-invasive, real-time, multi-channel imaging in living mice in video rate (27 frames per second, fps) was demonstrated. However, it was limited to three colors and produced some challenges in motion artifacts due to the ~10 ms separation between channels. Faster acquisition speeds would allow for enhanced temporal resolution in three-color imaging and/or increased number of orthogonal excitation channels (and thus biological parameters) that can be acquired while maintaining video-rate acquisition.

To produce orthogonal signals from differing, well-separated (~75–100 nm) excitation wavelengths across the NIR and SWIR regions, two classifications of emitters are necessary: (1) fluorophores with SWIR absorption and emission and (2) NIR-absorbing dyes which exhibit long wavelength emission tails

Received: November 10, 2020

Published: May 3, 2021



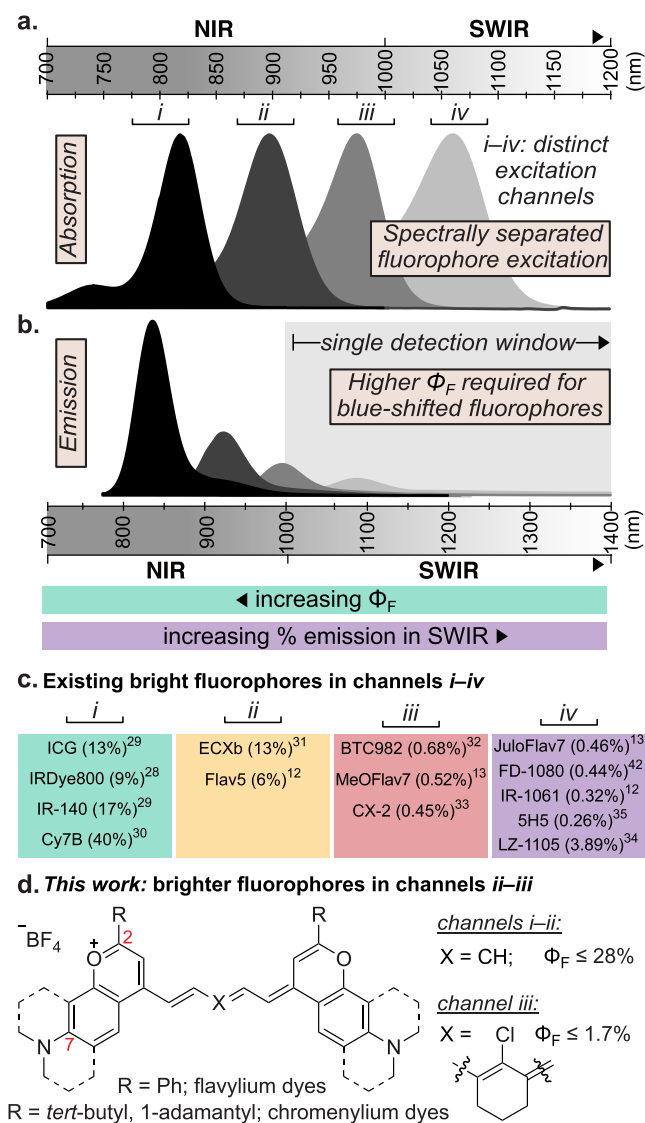


**Figure 1.** Fluorophores in the context of excitation multiplexed SWIR imaging. (a) Absorption properties of select fluorophores aligned with distinct excitation channels across the NIR and SWIR regions. (b) Emission properties of select fluorophores across the NIR and SWIR overlaid with a SWIR detection window, defined here as 1000–1700 nm. Intensities are schematized to represent the key imaging concepts defined below. (c) Existing fluorophores with high  $\Phi_F$  ( $\Phi_F$  in parentheses) values for their respective absorption wavelength aligned with the excitation channels defined in (a).<sup>49</sup> (d) Pentamethine and heptamethine fluorophores reported in this manuscript. Positions 2- and 7- on the flavylium and chromenylium heterocycles are indicated in red.

extending into the SWIR region (Figure 1). Imaging NIR dyes in the SWIR requires a higher overall brightness to compensate for the small fraction of the emission signal that is collected (Figure 1b). Fortunately, this concept aligns well with the energy gap laws,<sup>24</sup> allowing drastically higher fluorescence quantum yields ( $\Phi_F$ ) to be obtained with more blue-shifted dyes. However, apart from the FDA-approved indocyanine green<sup>25,26</sup> (ICG, Figure 1b), and analogues<sup>27–30</sup> which are commonly excited between 785–808 nm, currently, there are few bright probes with NIR absorption >800 nm (Figure 1c,ii,iii, Chart S1).<sup>12,13,31–35</sup> To improve both the speed and degree of multiplexing for non-invasive imaging in small animals, brighter

dyes with narrow excitation spectra at wavelengths between 800 and 1000 nm are necessary.

Small molecules are desirable contrast agents due to their small size, biocompatibility, and simple bioconjugation approaches.<sup>36</sup> Polymethine dyes, fluorophores composed of two heterocyclic terminal groups connected by a vinylene chain,<sup>37,38</sup> are ideal candidates for excitation multiplexing, as they have high absorption coefficients ( $\epsilon$ ), often above  $\sim 10^5$  M<sup>-1</sup> cm<sup>-1</sup>, and narrow absorption profiles which can be fine-tuned to match excitation channels.<sup>13,39</sup> While red-shifted polymethine dyes often retain favorable absorptive properties,  $\Phi_F$  values drop drastically in the NIR to SWIR regions.<sup>40</sup> As brightness is reliant on both absorptive and emissive properties (brightness =  $\epsilon_{\max} \times \Phi_F$ ;  $\epsilon_{\max}$  = absorbance coefficient at  $\lambda_{\max,abs}$ ), an ideal fluorophore will undergo both excitation and emission efficiently. Efforts to increase the quantum yield of polymethine fluorophores have included reducing nonradiative processes by interactions with biomolecules,<sup>25,41,42</sup> introducing conformational restraint on the polymethine chain,<sup>43,44</sup> or decreasing intersystem crossing by replacing heavy atoms.<sup>12,45</sup> Further efforts to increase brightness in polymethine dyes include reducing aggregation effects to increase the amount of actively absorbing and emitting species that can be detected.<sup>30,46,26</sup>

As a starting point to obtain NIR polymethine dyes with absorption maxima >800 nm and high brightness, we looked to the oxygen-containing flavylium dyes, which have previously furnished bright NIR and SWIR-light absorbing molecules. Fluorophores constructed from a 4-methyl-7-dimethylamino flavylium heterocycle include heptamethine dye 1 (Flav7,  $\lambda_{\max,abs} = 1027$  nm,  $\Phi_F \sim 0.5\%$ ) and pentamethine dye 2 (Flav5,  $\lambda_{\max,abs} = 862$  nm,  $\Phi_F \sim 5\%$ ),<sup>12</sup> (Figure 2a) which are  $\sim 10$ -fold more emissive than the thiaflavylium counterparts,<sup>30,47</sup> likely due to reduction in intersystem crossing (in addition to the effects of energy gap laws). Investigation of structure–property relationships by systematic substitution of the flavylium heterocycle produced trends which could reliably red- or blue-shift excitation wavelengths but did not produce significant enhancements in the emissive properties, offering little insight into further increasing the brightness of the scaffold.<sup>13,48</sup> Here, we explore structural features on the heterocycle that increase the emissive behavior in long wavelength polymethine dyes. The resulting dyes are applied to fast and multiplexed SWIR imaging in mice.

## RESULTS AND DISCUSSION

**Design, Synthesis, and Photophysical Characterization of SWIR-Emitting Polymethine Dyes.** We hypothesized that rotational and vibrational modes within the phenyl group at the 2-position on flavylium (Figure 1d) could be contributing to internal conversion in the resulting polymethine dyes. To investigate this question, we targeted 4-methyl chromenylium heterocycles containing either a *tert*-butyl or a 1-adamantyl group at their 2-positions and applied them to synthesize pentamethine and heptamethine dyes with absorption between 800 and 1000 nm (Figure 2a,b). We found that the chromenylium heterocycles could be synthesized by an analogous route to the prior flavylium variants<sup>13</sup> (Scheme S1). From these heterocycles, we synthesized the hepta- and pentamethine chromenylium dyes 5–8 (Figure 2a, Chart S2) through the classic polymethine condensation reaction with the corresponding conjugated bis(phenylimine) (S5 and S6, respectively, Scheme S1).

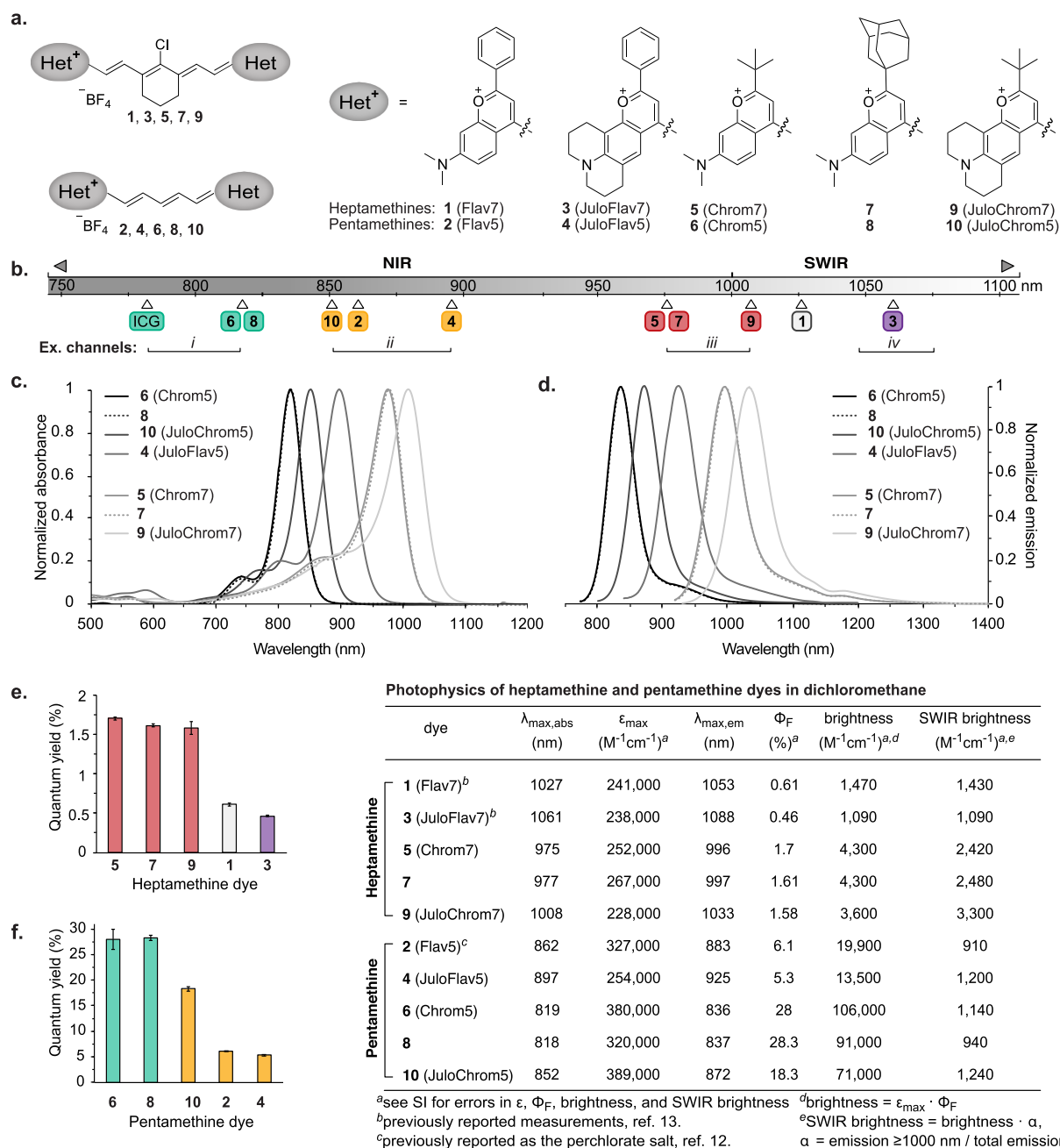


**Figure 2.** Structures and photophysical properties of heptamethine and pentamethine dyes. (a) Chemical structures of heptamethine and pentamethine dyes explored in this study (see Chart S2 for full structures). (b) Absorption maxima of ICG and dyes 1–10 displayed graphically on the electromagnetic spectrum and aligned with the distinct excitation channels used for excitation-multiplexed, single-channel SWIR imaging. (c) Absorbance spectra of newly reported dyes. (d) Emission spectra of newly reported dyes, ex. = 755 nm for pentamethine dyes; ex. = 885 nm for heptamethine dyes. (e, f) Quantum yields of heptamethine dyes (e) and pentamethine dyes (f) displayed graphically; error bars represent standard deviation. (g) Table of photophysical properties. See Table S1 for error values.

In previous work, we found that the introduction of a julolidine-containing flavylium heterocycle provided advantageous red-shifts (3, JuloFlav7,  $\lambda_{\max, \text{abs}} = 1061$  nm,  $\Phi_{\text{F}} \sim 0.46\%$ ) compared to Flav7 (1).<sup>13</sup> Consequently, we were also interested in investigating the pentamethine flavylium dye that would result from this same julolidine-containing heterocycle (4) and the chromenylium pentamethine and heptamethine fluorophores containing the julolidine functionality (9 and 10, respectively, Figure 2a).

After preparation of the chromenylium dyes 5–10 as well as the previously reported flavylium dyes 1–3 and the new

flavylium dye 4 (Scheme S2, select dyes are named after the heterocycle and the number of methine units in the polymethine chain), we performed a thorough comparative investigation of their photophysical properties. The photophysical properties in dichloromethane reveal that the absorption and emission of the chromenylium heptamethine derivatives are blue-shifted by  $\lambda \sim 52$  nm ( $\nu \sim 500$   $\text{cm}^{-1}$ ) and the chromenylium pentamethine dyes by  $\lambda \sim 44$  nm ( $\nu \sim 600$   $\text{cm}^{-1}$ ), from their flavylium counterparts (Figure 2b–d,g). The absorption coefficients remain characteristically high, with the pentamethine dyes having, on average, higher values than the heptamethine dyes, at

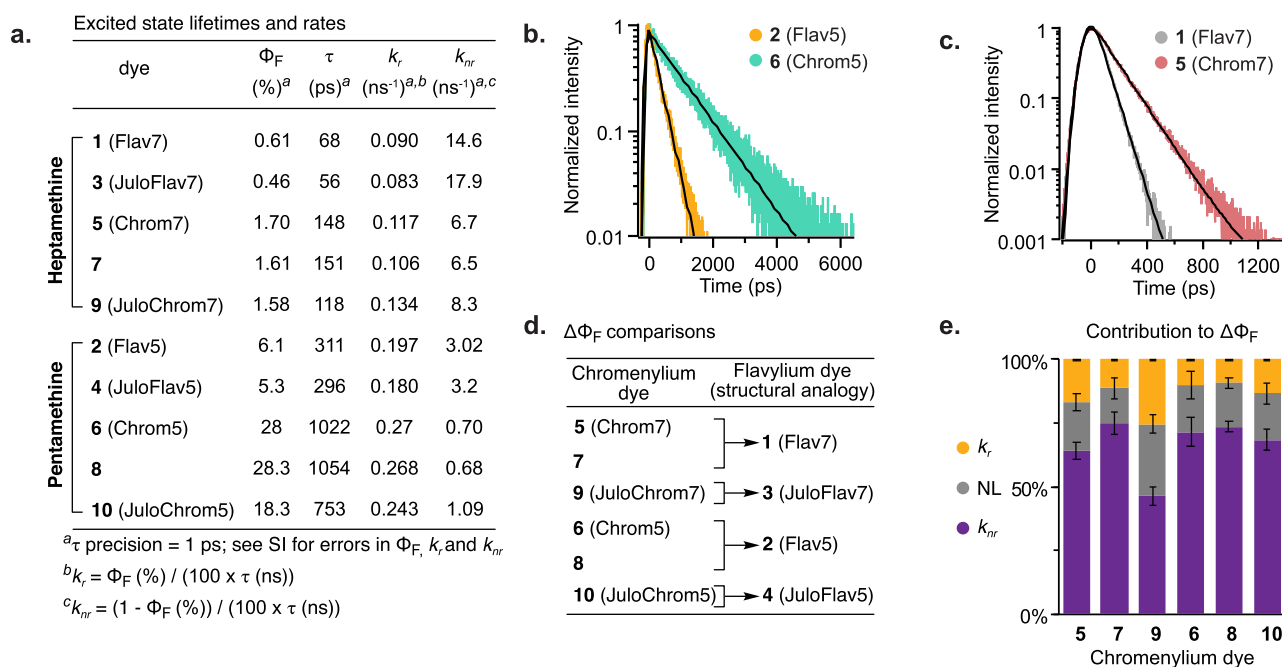


**Figure 3.** Analysis of heptamethine and pentamethine dye emissive properties. (a) Table of photoluminescence lifetimes and rates. (b, c) Time-correlated emission of selected dyes 2 and 6 (b) or 1 and 5 (c) and fitting curves. (d) Chart outlining comparisons made between chromenylum and flavylium dyes for  $\Delta\Phi_F$  analysis in (e). (e) Relative contribution of nonradiative rate ( $k_{nr}$ ), radiative rate ( $k_r$ ), or a nonlinear contribution (NL) composed of a combination of both  $k_{nr}$  and  $k_r$  to  $\Delta\Phi_F$  between chromenylum and flavylium dyes (Note S3).

$\sim 360,000 \text{ M}^{-1} \text{ cm}^{-1}$  and  $\sim 250,000 \text{ M}^{-1} \text{ cm}^{-1}$ , respectively (Figure 2g). Remarkably, the emissive properties were increased substantially, with heptamethine chromenylum dyes  $\Phi_F = 1.6\text{--}1.7\%$  (relative measurements to IR-26 = 0.05%)<sup>45</sup> and pentamethine chromenylum dyes  $\Phi_F = 18\text{--}28\%$  (absolute quantum yield measurements) (Figure 2e–g, Note S1). Combining the absorptive and emissive properties, 5 and 7 have the highest brightness of the heptamethines at  $4300 \text{ M}^{-1} \text{ cm}^{-1}$ , while 6 is the brightest pentamethine ( $106,000 \text{ M}^{-1} \text{ cm}^{-1}$ ).

When comparing brightness to current state of the art organic fluorophores with similar absorption wavelengths in each excitation channel (dyes outlined in Figure 1c, Table S2), the chromenylum dyes fare quite well. For example, in region (i), dye 6 is brighter than ICG,<sup>27</sup> IRDye-800,<sup>26</sup> and IR-140<sup>27</sup> and displays similar brightness to the conformationally restricted heptamethine indocyanine<sup>28</sup> (notated here as Cy7B). Dye 10 (in region ii) is  $\sim 3.5\text{--}$  and  $\sim 4\text{-fold}$  brighter than Flav5<sup>12</sup> and ECXb,<sup>29</sup> respectively, while dye 5 (in region iii) is between  $\sim 2.5\text{-}$  and  $5\text{-fold}$  brighter than the current standards BCT982,<sup>30</sup> MeOFlav7,<sup>13</sup> and CX-2.<sup>31</sup> Thus, the series of chromenylum dyes provide bright organic chromophores with NIR-absorption.

While overall brightness is an important comparative metric, the more relevant brightness metric for excitation-multiplexed imaging with single channel SWIR detection is the percent of emission that is within the SWIR region. We accounted for this parameter by defining SWIR brightness =  $\epsilon_{\text{max}} \times \Phi_F \times \alpha$ , where  $\alpha = \text{emission} \geq 1000 \text{ nm} / \text{total emission}$ , calculated from the emission spectra. All of the chromenylum heptamethine dyes have a higher SWIR brightness than the flavylium heptamethine dyes, despite their more blue-shifted photophysics (Figure 2g). For the pentamethines, flavylium dye 4 and chromenylum dyes 6 and 10 are the brightest SWIR emitters of the series.

### Investigation of Enhanced $\Phi_F$ of Chromenylum Dyes.

The chromenylum dyes display significant improvements in their  $\Phi_F$  compared to their flavylium analogues. To investigate this enhancement, we measured the fluorescence lifetimes ( $\tau$ ) of dyes 1–10 by time-correlated single-photon counting (TCSPC) (see Note S2). We found that in all cases,  $\tau$  increased considerably for the chromenylum dyes compared to the flavylium dyes, corresponding to the increase in  $\Phi_F$ . A  $\sim 2.5\text{-fold}$  increase in  $\tau$  to  $\sim 140 \text{ ps}$  for the heptamethines (5, 7, 9) and a  $\sim 3.1\text{-fold}$  enhancement to  $\tau \sim 1 \text{ ns}$  for the pentamethines 6 and 8 (Figures 3a–c) are observed. A slightly shorter  $\tau$  ( $\sim 750 \text{ ps}$ ), and corresponding lower  $\Phi_F$ , is determined for the more red-shifted pentamethine 10. By calculating the radiative ( $k_r$ ) and nonradiative ( $k_{nr}$ ) rates from these data, we discovered that while modest increases in  $k_r$  are observed for the brighter dyes, the  $k_{nr}$  are more drastically affected. There is an average of 2.3-fold decrease in  $k_{nr}$  for the heptamethines and a 3.8-fold decrease in  $k_{nr}$  for the pentamethines when comparing chromenylum to flavylium dyes (Figure 3a). This effect can be visualized by comparing analogous chromenylum and flavylium structures (Figure 3d) and observing the relative contribution of changes in  $k_r$  or  $k_{nr}$  to  $\Delta\Phi_F$  between the two scaffolds. (Figure 3e, Note S3). The finding that the decreased  $k_{nr}$  is the dominant contributor to the increased  $\Phi_F$  in the chromenylum dyes lead us to hypothesize that the bulky alkyl groups at the 2-position provide fewer vibrational modes that enable relaxation by internal conversion in the SWIR region as compared to a phenyl group. We are unable to decouple the vibrational mode effects from those imparted by the energy gap laws which state blue-shifted dyes will have both increased  $k_r$  and decreased  $k_{nr}$  compared to “vibrational mode equivalent” molecules with a smaller HOMO–LUMO gap.<sup>50</sup> Nonetheless, the significantly increased  $\Phi_F$  seen here, which is absent in other polymethine dyes with a similar wavelength of absorption, supports that

reducing vibrational modes is playing an important role in the increase in emissive behavior.

To further understand the differences between the two dye types, we obtained the X-ray crystal structures of dyes 4 and 5 as exemplars of the flavylium and chromenylium scaffolds, respectively (Figure 4). Focusing on the 2-position of the

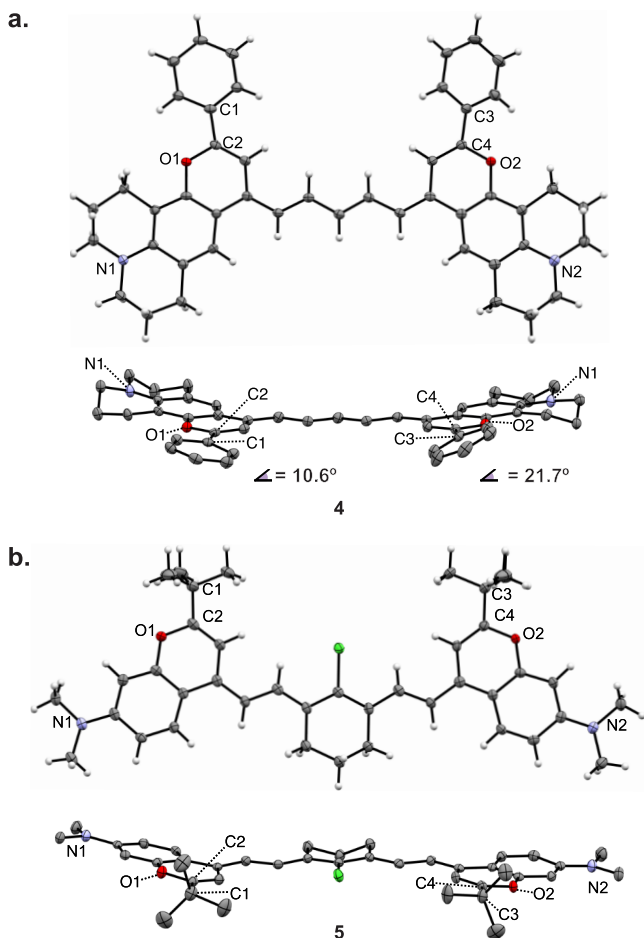


**Figure 4.** Thermal ellipsoid plots (ORTEP) for compound 4 (a) and 5 (b), arbitrary numbering, shown at two viewpoints. Counterions and solvent molecules are omitted for clarity. Lower structures omit all H atoms for clarity. Atomic displacement parameters are drawn at the 50% probability level.

heterocycle, the phenyl group on the flavylium dye 4 lies  $\sim 10\text{--}20^\circ$  out of plane of the polymethine chain, and the C1–C2 and C3–C4 bonds have an average bond length of 1.47 Å, indicating single bond C(sp<sup>2</sup>)–C(sp<sup>2</sup>) character. These metrics suggest that free rotation of the phenyl groups occur in solution and likely contribute to nonradiative decay.<sup>51</sup> Chromenylium dye 5 displays the expected C2–C1 and C4–C3 bond lengths of 1.51 Å for a C(sp<sup>2</sup>)–C(sp<sup>3</sup>) bond, also indicating rotational freedom. With the crystal structures suggesting rotation of the 2-position substituent in both fluorophores, it is likely that vibrational modes are the dominant contributor to the observed differences in  $k_{nr}$ .

#### Photostability of Chromenylium vs Flavylium Dyes.

Finally, we compared the photostability between the chromenylium and flavylium dyes (Note S4). Pentamethine dyes 2 and 6 were dissolved in DMSO and irradiated with 786 nm light ( $100\text{ mW cm}^{-2}$ ), while heptamethine dyes 1 and 5 were treated with 974 nm light ( $100\text{ mW cm}^{-2}$ ), and their emission intensity

was recorded over time. Comparing the chromenylium dyes to their flavylium counterparts, the pentamethine chromenylium dye 6 displayed slightly higher stability ( $\sim 1.7$  fold) compared to flavylium dye 2. In contrast, the heptamethine chromenylium dye 5 was less photostable ( $\sim 2.7$ -fold) than flavylium dye 1. We hypothesize that the reversal of the stability between the chromenylium and flavylium dyes observed for the heptamethine dyes results from 1 having minimal ability to sensitize oxygen.<sup>12</sup> Overall, the photostability of the chromenylium dyes is similar enough to that of the flavylium dyes that we expect minimal impact on macroscopic *in vivo* imaging experiments, where dye concentrations are relatively high.

**In Vitro Comparative Brightness Experiments.** While photophysical characterization is essential for understanding chromophore properties, there are many additional parameters that contribute to a dye's *in vivo* performance, including delivery strategy, interaction with biological tissues, and the excitation and detection parameters of the imaging setup. To begin to understand the translation to *in vivo* experiments, we used an excitation-multiplexed SWIR imaging configuration to compare emission of the fluorophores in different biologically relevant media when excited at different wavelengths. The imaging setup includes excitation lasers that correspond to each channel (*i–iv*, Figure 1a) (785, 892, 968, and 1065 nm), which are diffused and delivered uniformly to the biological sample. Excitation irradiation is scaled to the approved values, as outlined by the International Commission on Non-Ionizing Radiation Protection (ICNIRP) guidelines. The guidelines indicate that within the spectral region ( $\sim 785\text{--}1065\text{ nm}$ ), higher photon doses are tolerated as the wavelength is increased. This results in a factor of 3.4-fold higher irradiation power allowed at 1000 nm compared to 785 nm.<sup>52</sup> Importantly, the excitation-multiplexed imaging configuration provides fast switching of the excitation lasers (on the  $\mu\text{s}$  time scale), allowing for real-time multicolor imaging. Collection is achieved through a single-channel (“color-blind”) SWIR detector that records individual frames for each excitation channel in tandem. Multiplexed frames are obtained by merging the adjacent frames from each excitation channel. As multiplexed frame rates are related to the exposure time multiplied by the number of channels used in the experiment, to obtain video-rate speeds, bright probes and short exposure times are necessary.

To compare brightness of the chromenylium dyes *in vitro*, we first dissolved dyes 5, 6, 9, and 10, in organic solvent (DCM) at  $0.25\ \mu\text{M}$ , and measured the emission with 1000 nm long-pass (LP) filtering on an InGaAs camera upon sequential excitation with 785, 892, and 968 nm lasers. ICG (in EtOH), 4, and MeOFlav7 were used as benchmarks for excitation channels, *i–iii*, respectively. When the raw count data are normalized to the exposure time used in image collection, it is clear that 5, in channel *iii*, produces the brightest SWIR emission in organic solvent with excitation with the 968 nm laser, providing a  $\sim 3$ -fold advantage in brightness over MeOFlav7, previously employed for three-color imaging.<sup>13</sup> The other two channels offered a lower signal overall, but the best performers in channels *i* and *ii* were ICG and 4, respectively (Figure S1).

Next, to more closely approximate *in vivo* performance, we formulated each chromenylium or flavylium dye into water-soluble poly(ethylene) glycol-phospholipid micelles, a biocompatible nanomaterial for delivery (Scheme S3). Upon lipid encapsulation by probe sonication and washing with PBS, the resulting micelles of dyes 3, 4, 5, and 10 were  $\sim 15\text{--}20\text{ nm}$  in size, while micelles composed of dye 6 were larger at  $\sim 40\text{ nm}$

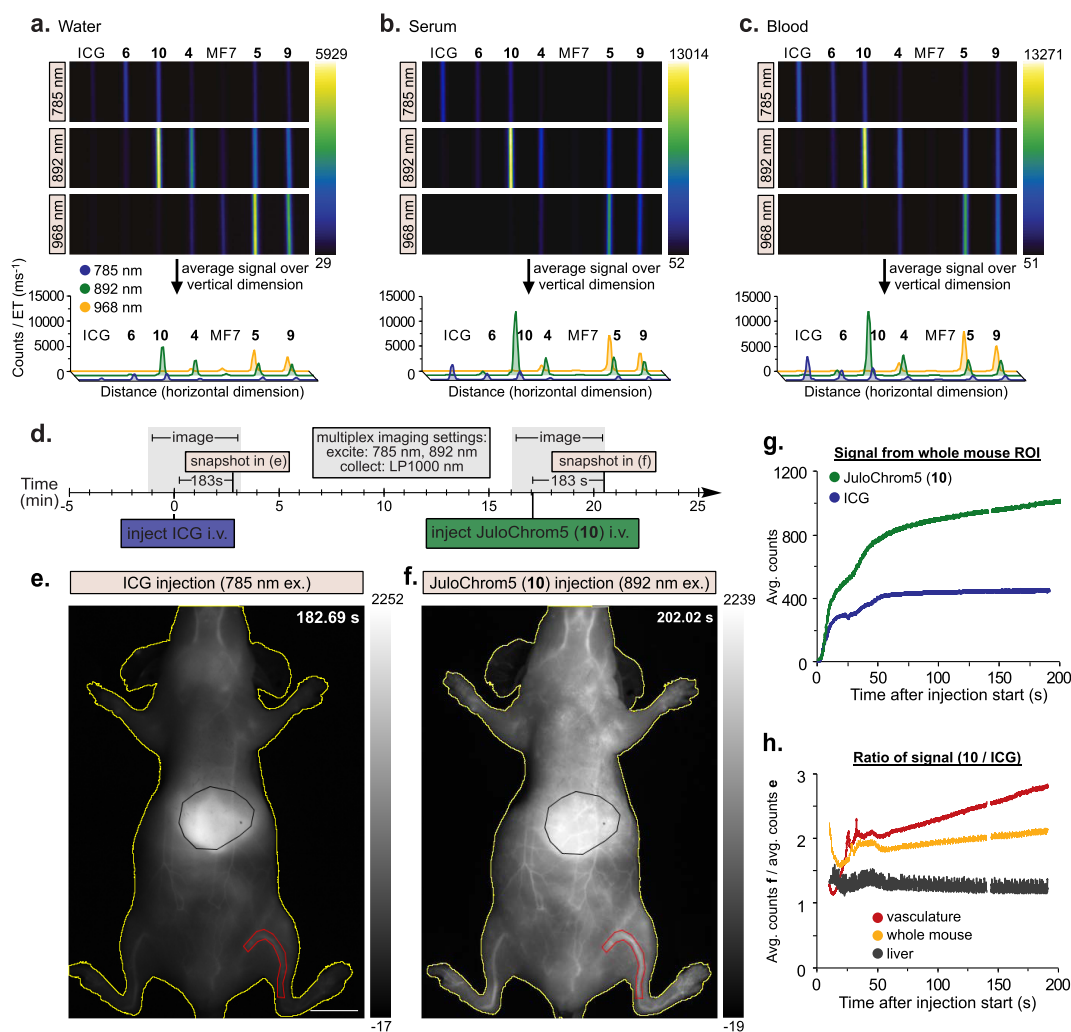


**Figure 5.** Brightness comparisons in imaging configuration. (a–c) Images upon 785 ( $33 \text{ mW cm}^{-2}$ ), 892 ( $54 \text{ mW cm}^{-2}$ ), and 968 ( $77 \text{ mW cm}^{-2}$ ) nm ex. and LP1000 nm detection (variable ET and frame rate) of capillaries containing equal moles of dyes 4–6, 9, 10 (lipid formulations) and benchmark dyes ICG (free) and MeOFlav7 (abbreviated MF7, lipid formulation) when dissolved in water (a), FBS (b), or sheep blood (c). Displayed images were averaged over 200 frames and normalized to the ET used in each image. The intensities are averaged over the vertical dimension and are plotted over distance in the horizontal dimension below each image. (d) Experimental timeline for the imaging experiment in (e, f). (e, f) Images after injection of ICG (50 nmol) upon 785 nm ( $64 \text{ mW cm}^{-2}$ ) ex. (e) and after injection of JuloChrom5 (10) (50 nmol) upon 892 nm ( $104 \text{ mW cm}^{-2}$ ) ex. (f). Collect: LP1000 nm, 2.0 ms ET, 150 fps (for two-channel collection, see Figure S7 for cross-talk evaluation). Single frames at the time point which displayed the highest intensity over the whole mouse ROI obtained during acquisition are displayed. (g) Intensity quantification from images in (e, f) taken by averaging intensity over the whole mouse at each frame after i.v. injection, where  $t = 0$  is the initial frame in which signal is visualized. (h) Ratio of intensities (JuloChrom5 (10)/ICG) from ROIs quantified in (e, f). Scale bar = 1 cm.

(Figure S2). The surface charge of the micelles was between  $-6$  and  $-13$  mV (Figure S2). Interestingly, while the formation of non-emissive aggregates in addition to a monomer species is common for encapsulated long wavelength polymethine dyes, the chromenylum dyes 5, 6, 9, and 10 display minimal aggregate formation in their UV–vis–NIR absorption spectra (Figure S3).

To compare brightness between dyes, solutions with equal dye concentration (flavylium and chromenylum dyes in micelles; ICG, free; see Note S5) were dispersed in water (Figure 5a), fetal bovine serum (FBS) (Figure 5b), and sheep blood (Figure 5c) and loaded into capillary tubes (Figure S4). As many polymethine dyes, most notably ICG,<sup>53</sup> are known to increase in brightness in serum and blood, it is essential to perform benchmarking experiments in these biologically relevant media. Evaluating brightness in these media changed the results drastically compared to those in the organic solvent experiment, likely due to variable amounts of aggregation or

interactions within the micelles and/or biological media. Notably, in all media, two dyes stand out with significantly high SWIR brightness, 10, when excited with the 892 nm laser, and 5, when excited with the 968 nm laser. While ICG is the brightest SWIR emitter upon 785 nm laser excitation in both FBS and blood, both chromenylum dyes produce a greater signal in their respective channels (*ii* and *iii*) compared to that of ICG (in channel *i*). In blood, the most representative media, this quantitates to a  $\sim 2.8$ -fold and  $\sim 1.7$ -fold improvement in signal over ICG for 10 and 5 respectively. Additionally, comparing the performance of the chromenylum dyes between media, it is clear that, similar to ICG, an increase in brightness is occurring in FBS and blood compared to water. Interestingly, the opposite effect is observed for MeOFlav7, likely due to instability in these more complex environments. Similar experiments using either equal laser power or equal photon number at all excitation wavelengths have an expected reduced performance at the

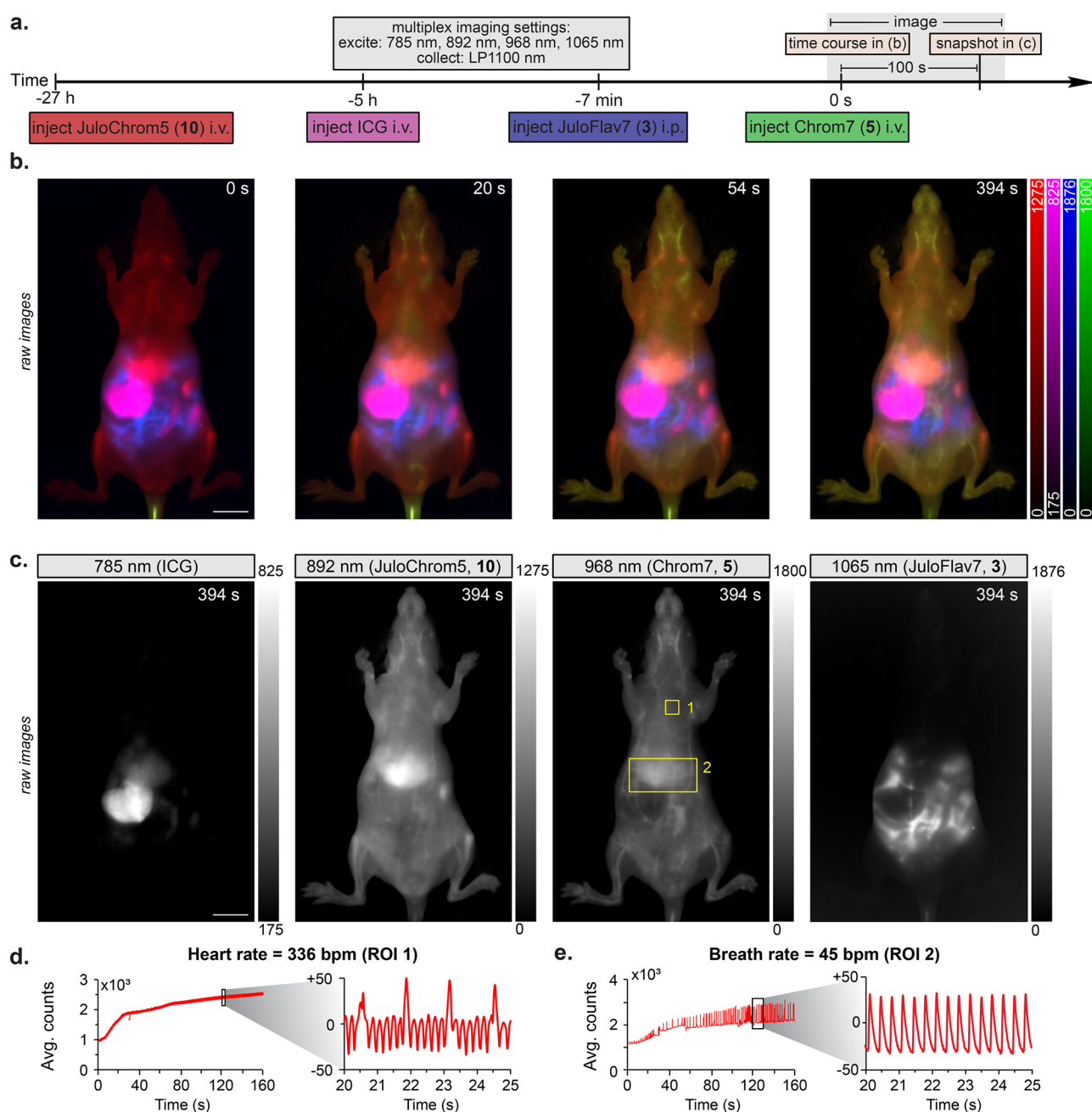


**Figure 6.** Video-rate four-color imaging. (a) Experimental timeline for experiment in (b, c) (not to scale). (b, c) Composite images (b) and single frames (c) from four-color excitation multiplexed SWIR imaging at 30 fps. Injection amounts are as follows: ICG = 200 nmol; JuloChrom5 (**10**) = 50 nmol; Chrom7 (**5**) = 45 nmol; JuloFlav7 (**3**) = 45 nmol. Ex. 785 nm ( $45 \text{ mW cm}^{-2}$ ), 892 nm ( $75 \text{ mW cm}^{-2}$ ), 968 nm ( $103 \text{ mW cm}^{-2}$ ), 1065 nm ( $156 \text{ mW cm}^{-2}$ ); collect LP1100 nm, 7.8 ms, 30 fps, single frames are displayed. (d, e) Heart rate (d) and breath rate (e) calculated from ROIs specified in (c). Scale bar = 1 cm.

longer excitation wavelengths compared to those using ICNIRP-suggested powers, but still predict a  $\sim 2$ -fold brightness advantage of **10** over ICG (Figures S5 and S6). As **5** and **10** will be further applied in multiplexed SWIR imaging, we will refer to them as Chrom7 (**5**) and JuloChrom5 (**10**), respectively, in the *in vivo* experiments.

**Comparative *In Vivo* Imaging Experiment.** To most closely assess the brightness performance for SWIR imaging, we designed an *in vivo* comparative experiment between the highest performing chromenylum dye, JuloChrom5 (**10**), and ICG. To note, while many SWIR imaging agents have been compared to the benchmark dye, ICG, these comparisons are often difficult

due to the diverse photophysical and biological properties of different emitters. In our case, the *in vivo* comparison is complicated by differing biodistribution properties of the two dyes. ICG, delivered as a free dye, has a faster rate of clearance from the blood into the liver than JuloChrom5 (**10**), delivered encapsulated in poly(ethylene) glycol-phospholipid micelles. While this difference cannot be entirely decoupled from the conclusions, we aimed to reduce uncertainty in other aspects of the experiment and the analysis. We capitalized on the multiplexing capabilities of the two dyes to perform a comparative experiment of both agents in a single mouse, thus reducing biological sample variance. As the signal from ICG

upon 892 nm laser irradiation is negligible with these acquisition settings (Figure S7), we performed temporally separated tail-vein injections of equal moles of ICG, followed by JuloChrom5 (10) into mice and imaged each injection in two channels, with 785 and 892 nm lasers and collection with 1000 nm LP filtering (Figure 5d–f, Figure S8). Normalizing each acquisition to the injection start time, we quantified the signal over time over the whole mouse (yellow), a section of the vasculature (red), and the liver (black). Looking at the whole mouse region of interest (ROI) (Figure 5g), the signal from JuloChrom5 (10) is significantly higher than the signal from ICG. However, the ratio of counts between 10 and ICG (Figure 5h) increases when looking only at the vasculature. Conversely, the ratio (10 to ICG) decreases when observing the liver, due to the faster hepatic clearance time of ICG compared to the PEG-coated micelles containing 10. Despite this difference, 10 still demonstrates a slightly higher signal than ICG in the liver over the observed time frame. While differential biodistribution could result in variable probe depths and differing amounts of attenuation, the higher signal among several regions of interest *in vivo*, combined with the more controlled *in vitro* quantification, leads us to conclude that JuloChrom5 (10) displays an overall higher signal in the SWIR compared to ICG. Importantly, the advantageous brightness of 10 enables imaging with high signal-to-noise ratios (SNR) at low exposure times (1.6–2.0 ms) (Figure S9). Accordingly, we can now image a whole mouse in a single color at frame rates up to 300 fps, limited by the collection rate of the current detector. Notably, the more red-shifted dye, Chrom7 (5), in channel *iii*, can also be employed to image in a single color at 300 fps, with good SNR and similar acquisition parameters (Figure S10, Video S1), enabling rapid, multiplexed SWIR imaging.

**Fast, Multiplexed *In Vivo* SWIR Imaging.** We next moved to examine how the brighter dyes can be used to improve excitation-multiplexed, single-channel detection SWIR imaging. Previously, we demonstrated three-color imaging in real time (up to 27 fps).<sup>13</sup> Here, we aimed to improve the temporal resolution of the method as well as increase the number of channels at which orthogonal signals can be detected. The high brightness of the chromenylum dyes and the flavylum pentamethine dyes, coupled with the varied absorption profiles across the NIR, provides several candidate dyes for multiplexed imaging using channels *i–iii*. First, we used 6 (referred to here as Chrom5), 4 (referred to here as JuloFlav5), and Chrom7 (5) together, preferentially excited by 785, 892, and 968 nm lasers, respectively, with collection using 1000 nm LP filtering. The three dyes were injected at differing times or routes to ensure varied biodistribution of the different channels during imaging. The injection amounts of each dye were optimized to provide similar brightness using the ICNIRP-scaled power densities. Images with excellent signal (Figure S11, Video S2) were collected with 3.3 ms exposure time (ET) and 100 fps multiplexed frame rate (multiplexed frame rate =  $1/(n \times ET)$ , where  $n$  = number of channels), which is over 3× the speed obtained previously.<sup>13</sup> Multiplexing at these high frame rates ensures that macroscopic biological motion is negligible within the collection time for each frame that contributes to the composite image and will offer increased benefits in applications such as image-guided surgery or imaging animals in the absence of anesthesia.

Finally, the new NIR fluorophores allowed the addition of a fourth channel such that four-color SWIR imaging could be performed for the first time. We chose ICG, JuloChrom5 (10),

Chrom7 (5), and JuloFlav7 (3) as spectrally distinct fluorophores with preferential excitation at 785, 892, 968, and 1065 nm, respectively, and collection with 1100 nm LP filtering (Figure 6a, Figures S12–S14, Video S3). Again, we optimized injection routes, times, and amounts to ensure a different biodistribution of probes would be present with similar brightness at the time of imaging. First, JuloChrom5 (10) was injected *i.v.* 27 h prior to serve as a structural reference. Next, ICG was injected *i.v.* and allowed to clear for 5 h through the liver into the intestine. JuloFlav7 was then administered into the *i.p.* space 7 min before imaging, and finally, Chrom7 (5) was injected *i.v.* to obtain the time-course images of the injection displayed in Figure 6b,c. For multiplexed experiments employing 1065 nm laser excitation, longer exposure times were needed due to the smaller, more red-shifted collection window decreasing the percentage of emissive-tails of the dyes collected. Nonetheless, the signal in each channel was sufficient for collection at 30 fps, with a 7.8 ms ET for each channel. Notably, the four-color experiment was able to be performed at similar speeds to previously reported three-color experiments which used 1064 nm laser excitation, providing video-rate temporal resolution of function, visualized in the heart and breathing rates (Figure 6d,e).<sup>13</sup> The lower exposure times used herein (7.8 ms vs 10 ms) were possible due to the improved brightness of the chromenylum dyes and the scaled power densities of the excitation wavelengths.<sup>13</sup> Additionally, a linear unmixing procedure accommodating four-color data can reduce cross talk for visualization (Figure S12, Note S6). The improvements in imaging speed and number of channels open up opportunities to monitor multiple anatomical (such as lymphatic, hepatic, and skeletal) and functional (such as metabolic) parameters simultaneously, on a millisecond time scale. The fast speeds provided will be essential for imaging in applications with significant macroscopic motion, that is, for intraoperative and awake, unrestrained animal imaging. Further work to transform dyes into molecular imaging probes will enable specific biomolecule localization of multiple probes in a single animal in combination with anatomical references.

## CONCLUSION

The ability to non-invasively and longitudinally track multiple probes within living animals will be key to studying causes and interventions of human disease. Fluorescence is an optimal tool for high-resolution and high-sensitivity detection, but non-invasive experiments are limited by light scattering in tissue. Longer wavelength detection benefits from increased penetration depth and contrast, but lacks bright enough probes that can be concurrently detected orthogonally. Here, we designed and synthesized seven new polymethine dyes with flavylum or chromenylum heterocycles, which are brighter than their predecessors. The pentamethine and heptamethine chromenylum dyes benefit from significantly higher quantum yields due to decreased nonradiative rates compared to the flavylum dyes. We capitalize on the excitation-multiplexed strategy to compare performance and biodistribution of two probes in the same mouse. In this experiment, we found that JuloChrom5 (10), excitable at 892 nm, is brighter than ICG for *in vivo* experiments. The panel of bright dyes enables single-channel imaging at up to 300 fps, while dyes excitable at orthogonal excitation wavelengths can be used together providing three-channel imaging at up to 100 fps. These experiments represent the fastest single and multichannel SWIR imaging to date. Combining these dyes with ICG and JuloFlav7 (3), video-rate imaging in mice in four colors

is demonstrated for the first time. The contribution puts forth a greater understanding of how to increase the performance and utility of long wavelength probes to visualize complex organisms. Specifically, by improving the brightness of dyes in key wavelength regions and integrating their use into excitation-multiplexed SWIR imaging, we open up opportunities for non-invasive and high-resolution imaging of multiple biological parameters *in vivo*.

## ■ ASSOCIATED CONTENT

### SI Supporting Information

The Supporting Information is available free of charge at <https://pubs.acs.org/doi/10.1021/jacs.0c11599>.

Charts S1 and S2, Schemes S1–S3, Tables S1–S6, Figures S1–S18, Notes S1–S6, experimental procedures, and syntheses and characterization for all new compounds (PDF)

Video S1: Single color imaging at 300 fps (MOV)

Video S2: High-speed three-color imaging (MOV)

Video S3: Video rate four-color imaging (MOV)

### Accession Codes

CCDC 2050461–2050462 contain the supplementary crystallographic data for this paper. These data can be obtained free of charge via [www.ccdc.cam.ac.uk/data\\_request/cif](http://www.ccdc.cam.ac.uk/data_request/cif), or by emailing [data\\_request@ccdc.cam.ac.uk](mailto:data_request@ccdc.cam.ac.uk), or by contacting The Cambridge Crystallographic Data Centre, 12 Union Road, Cambridge CB2 1EZ, UK; fax: +44 1223 336033.

## ■ AUTHOR INFORMATION

### Corresponding Authors

Ellen M. Sletten – Department of Chemistry and Biochemistry, University of California, Los Angeles, Los Angeles, California 90095, United States; [orcid.org/0000-0002-0049-7278](https://orcid.org/0000-0002-0049-7278); Email: [Sletten@chem.ucla.edu](mailto:Sletten@chem.ucla.edu)

Oliver T. Bruns – Helmholtz Pioneer Campus, Helmholtz Zentrum München, D-85764 Neuherberg, Germany; School of Medicine, Technical University Munich, D-80333 München, Germany; Email: [Oliver.bruns@helmholtz-muenchen.de](mailto:Oliver.bruns@helmholtz-muenchen.de)

### Authors

Emily D. Cosco – Department of Chemistry and Biochemistry, University of California, Los Angeles, Los Angeles, California 90095, United States; Helmholtz Pioneer Campus, Helmholtz Zentrum München, D-85764 Neuherberg, Germany; [orcid.org/0000-0002-9902-6176](https://orcid.org/0000-0002-9902-6176)

Bernardo A. Arús – Helmholtz Pioneer Campus, Helmholtz Zentrum München, D-85764 Neuherberg, Germany; [orcid.org/0000-0001-6132-7793](https://orcid.org/0000-0001-6132-7793)

Anthony L. Spearman – Department of Chemistry and Biochemistry, University of California, Los Angeles, Los Angeles, California 90095, United States

Timothy L. Atallah – Department of Chemistry and Biochemistry, University of California, Los Angeles, Los Angeles, California 90095, United States

Irene Lim – Department of Chemistry and Biochemistry, University of California, Los Angeles, Los Angeles, California 90095, United States

Olivia S. Leland – Department of Chemistry and Biochemistry, University of California, Los Angeles, Los Angeles, California 90095, United States

Justin R. Caram – Department of Chemistry and Biochemistry, University of California, Los Angeles, Los Angeles, California 90095, United States; [orcid.org/0000-0001-5126-3829](https://orcid.org/0000-0001-5126-3829)

Thomas S. Bischof – Helmholtz Pioneer Campus, Helmholtz Zentrum München, D-85764 Neuherberg, Germany

Complete contact information is available at: <https://pubs.acs.org/doi/10.1021/jacs.0c11599>

### Notes

Image data sets, including all raw and processed imaging data generated in this work, are available at BioImage Archive, accession number: S-BIAD53. These data can be obtained free of charge via <https://www.ebi.ac.uk/biostudies/studies/S-BIAD53>. Custom software used in this manuscript can be found at GitLab. The software can be accessed free of charge via <https://gitlab.com/brunslab/ccda>.

The authors declare no competing financial interest.

## ■ ACKNOWLEDGMENTS

The authors thank the NSF (NSF GFRP DGE-1144087 to E.D.C.), the DOE (DE-SC0019245 to J.R.C.), the NIH (1R01EB027172 to E.M.S.), the Foote Family (E.D.C.), the Alfred P. Sloan Foundation (FG-2018-10855 to E.M.S.), the Emmy-Noether-Program of DFG (BR 5355/2-1 to O.T.B.), UCLA, and the Helmholtz Pioneer Campus Institute for Biomedical Engineering for financial support. The work was supported by shared instrumentation grants from the NSF (CHE-1048804) and NIH (1S10OD016387). The authors appreciate assistance from the Garcia Garibay lab (UCLA) for FTIR instrumentation, Jordan Dotson (UCLA) for crystallization, Saeed Khan (UCLA) for X-ray crystallography, Daniel Estabrook (UCLA) for  $\zeta$  measurements, and Martin Warmer (HPC), Jakob Lingg (HPC), and Mara Saccomano (HPC) for helpful discussions.

## ■ ABBREVIATIONS

DCM, dichloromethane; ET, exposure time; FBS, fetal bovine serum; FDA, United States Food and Drug Administration; fps, frames per second; ICG, indocyanine green; ICNIRP, International Commission on Non-Ionizing Radiation Protection; i.p., intraperitoneal; i.v., intravenous; LP, long-pass; MF7, MeO-Flav7; NIR, near-infrared; NL, nonlinear; ORTEP, Oak Ridge Thermal Ellipsoid Plot; ROI, region of interest; SNR, signal-to-noise ratio; SWIR, shortwave infrared; TCSPC, time-correlated single-photon counting; VIS, visible

## ■ REFERENCES

- (1) Bashkatov, A. N.; Genina, E. A.; Kochubey, V. I.; Tuchin, V. V. Optical properties of human skin, subcutaneous and mucous tissues in the wavelength range from 400 to 2000 nm. *J. Phys. D: Appl. Phys.* **2005**, *38*, 2543–2555.
- (2) Zhang, H.; Salo, D.; Kim, D. M.; Komarov, S.; Tai, Y.; Berezin, M. Y. Penetration depth of photons in biological tissues from hyperspectral imaging in shortwave infrared in transmission and reflection geometries. *J. Biomed. Opt.* **2016**, *21*, 126006.
- (3) Lim, Y. T.; Kim, S.; Nakayama, A.; Stott, N. E.; Bawendi, M. G.; Frangioni, J. V. Selection of quantum dot wavelengths for biomedical assays and imaging. *Mol. Imaging* **2003**, *2*, 50–64.
- (4) Carr, J. A.; Aellen, M.; Franke, D.; So, P. T. C.; Bruns, O. T.; Bawendi, M. G. Absorption by Water Increases Fluorescence Image Contrast of Biological Tissue in the Shortwave Infrared. *Proc. Natl. Acad. Sci. U. S. A.* **2018**, *115*, 9080–9085.
- (5) Welscher, K.; Liu, Z.; Sherlock, S. P.; Robinson, J. T.; Chen, Z.; Daranciang, D.; Dai, H. A route to brightly fluorescent carbon

nanotubes for near-infrared imaging in mice. *Nat. Nanotechnol.* **2009**, *4*, 773–780.

(6) Ceppi, L.; Bardhan, N. M.; Na, Y.; Siegel, A.; Rajan, N.; Fruscio, R.; Del Carmen, M. G.; Belcher, A. M.; Birrer, M. J. Real-time single-walled carbon nanotube-based fluorescence imaging improves survival after debulking surgery in an ovarian cancer model. *ACS Nano* **2019**, *13*, 5356–5365.

(7) Hong, G.; Robinson, J. T.; Zhang, Y.; Diao, S.; Antaris, A. L.; Wang, Q.; Dai, H. *In vivo* fluorescence imaging with Ag<sub>2</sub>S quantum dots in the second near-infrared region. *Angew. Chem., Int. Ed.* **2012**, *51*, 9818–9821.

(8) Bruns, O. T.; Bischof, T. S.; Harris, D. K.; Franke, D.; Shi, Y.; Riedemann, L.; Bartelt, A.; Jaworski, F. B.; Carr, J. A.; Rowlands, C. J.; et al. Next-generation *in vivo* optical imaging with short-wave infrared quantum dots. *Nat. Biomed. Eng.* **2017**, *1*, 0056.

(9) Naczynski, D. J.; Tan, M. C.; Zevon, M.; Wall, B.; Kohl, J.; Kulesa, A.; Chen, S.; Roth, C. M.; Riman, R. E.; Moghe, P. V. Rare-earth-doped biological composites as *in vivo* shortwave infrared reporters. *Nat. Commun.* **2013**, *4*, 2199.

(10) Zhong, Y.; Ma, Z.; Wang, F.; Wang, X.; Yang, Y.; Liu, Y.; Zhao, X.; Li, J.; Du, H.; Zhang, M.; et al. *In vivo* molecular imaging for immunotherapy using ultra-bright near-infrared-IIb rare-earth nanoparticles. *Nat. Biotechnol.* **2019**, *37*, 1322–1331.

(11) Yang, Q.; Ma, Z.; Wang, H.; Zhou, B.; Zhu, S.; Zhong, Y.; Wang, J.; Wan, H.; Antaris, A.; Ma, R.; et al. Rational Design of Molecular Fluorophores for Biological Imaging in the NIR-II Window. *Adv. Mater.* **2017**, *29*, 1605497.

(12) Cosco, E. D.; Caram, J. R.; Bruns, O. T.; Franke, D.; Day, R. A.; Farr, E. P.; Bawendi, M. G.; Sletten, E. M. Flavylium Polymethine fluorophores for near- and shortwave infrared imaging. *Angew. Chem., Int. Ed.* **2017**, *56*, 13126–13129.

(13) Cosco, E. D.; Spearman, A. L.; Ramakrishnan, S.; Lingg, J. P. G.; Saccomano, M.; Pengshung, M.; Arús, B. A.; Wong, K. C. Y.; Glasl, S.; Ntziachristos, V.; Warmer, M.; McLaughlin, R. R.; Bruns, O. T.; Sletten, E. M. Shortwave infrared polymethine fluorophores matched to excitation lasers enable noninvasive, multicolor *in vivo* imaging in real time. *Nat. Chem.* **2020**, *12*, 1123–1130.

(14) Zhu, S.; Herraiz, S.; Yue, J.; Zhang, M.; Wan, H.; Yang, Q.; Ma, Z.; Wang, Y.; He, J.; Antaris, A. L.; et al. 3D NIR-II molecular imaging distinguishes targeted organs with high-performance NIR-II bioconjugates. *Adv. Mater.* **2018**, *30*, 1705799.

(15) Wan, H.; Yue, J.; Zhu, S.; Uno, T.; Zhang, X.; Yang, Q.; Yu, K.; Hong, G.; Wang, J.; Li, L.; et al. A bright organic NIR-II manifold fluorophore for three-dimensional imaging into biological tissues. *Nat. Commun.* **2018**, *9*, 1171.

(16) Zhu, S.; Yang, Q.; Antaris, A. L.; Yue, J.; Ma, Z.; Wang, H.; Huang, W.; Wan, H.; Wang, J.; Diao, S.; et al. Molecular imaging of biological systems with a clickable dye in the broad 800- to 1,700-nm near-infrared window. *Proc. Natl. Acad. Sci. U. S. A.* **2017**, *114*, 962–967.

(17) Zubkovs, V.; Antonucci, A.; Schuergers, N.; Lambert, B.; Latini, A.; Ceccarelli, R.; Santinelli, A.; Rogov, A.; Ciepielewski, D.; Boghossian, A. A. Spinning-disc confocal microscopy in the second near-infrared window (NIR-II). *Sci. Rep.* **2018**, *8*, 13770.

(18) Wang, F.; Wan, H.; Ma, Z.; Zhong, Y.; Sun, Q.; Tian, Y.; Qu, L.; Du, H.; Zhang, M.; Li, L.; et al. Light-sheet microscopy in the near-infrared II window. *Nat. Methods* **2019**, *16*, 545–552.

(19) Hu, Z.; Fang, C.; Li, B.; Zhang, Z.; Cao, C.; Cai, M.; Su, S.; Sun, X.; Shi, X.; Li, C.; et al. First-in-Human Liver-Tumour Surgery Guided by Multispectral Fluorescence Imaging in the Visible and near-Infrared-I/II Windows. *Nat. Biomed. Eng.* **2020**, *4*, 259–271.

(20) Carr, J. A.; Valdez, T. A.; Bruns, O. T.; Bawendi, M. G. Using the Shortwave Infrared to Image Middle Ear Pathologies. *Proc. Natl. Acad. Sci. U. S. A.* **2016**, *113*, 9989–9994.

(21) Williams, S. J.; Prescher, J. A. Building Biological Flashlights: Orthogonal Luciferases and Luciferins for *in Vivo* Imaging. *Acc. Chem. Res.* **2019**, *52*, 3039–3050.

(22) Lu, G. J.; Farhadi, A.; Szablowski, J. O.; Lee-Gosselin, A.; Barnes, S. R.; Lakshmanan, A.; Bourdeau, R. W.; Shapiro, M. G. Acoustically

Modulated Magnetic Resonance Imaging of Gas-Filled Protein Nanostructures. *Nat. Mater.* **2018**, *17*, 456–463.

(23) Chen, M.; Knox, H. J.; Tang, Y.; Liu, W.; Nie, L.; Chan, J.; Yao, J. Simultaneous Photoacoustic Imaging of Intravascular and Tissue Oxygenation. *Opt. Lett.* **2019**, *44*, 3773.

(24) Thimsen, E.; Sadtler, B.; Berezin, M. Y. Shortwave-infrared (SWIR) emitters for biological imaging: a review of challenges and opportunities. *Nanophotonics* **2017**, *6*, 1043–1054.

(25) Carr, J. A.; Franke, D.; Caram, J. R.; Perkinson, C. F.; Saif, M.; Askoxylakis, V.; Datta, M.; Fukumura, D.; Jain, R. K.; Bawendi, M. G.; et al. Shortwave infrared fluorescence imaging with the clinically approved near-infrared dye indocyanine green. *Proc. Natl. Acad. Sci. U. S. A.* **2018**, *115*, 4465–4470.

(26) Starosolski, Z.; Bhavane, R.; Ghaghada, K. B.; Vasudevan, S. A.; Kaay, A.; Annapragada, A. Indocyanine green fluorescence in second near-infrared (NIR-II) window. *PLoS One* **2017**, *12*, No. e0187563.

(27) Zhu, S.; Hu, Z.; Tian, R.; Yung, B. C.; Yang, Q.; Zhao, S.; Kiesewetter, D. O.; Niu, G.; Sun, H.; Antaris, A. L.; et al. Repurposing cyanine NIR-I dyes accelerates clinical translation of near-infrared-II (NIR-II) bioimaging. *Adv. Mater.* **2018**, *30*, 1802546.

(28) Luciano, M. P.; Crooke, S. N.; Nourian, S.; Dingle, I.; Nani, R. R.; Kline, G.; Patel, N. L.; Robinson, C. M.; Diflippantonio, S.; Kalen, J. D.; et al. A nonaggregating heptamethine cyanine for building brighter labeled biomolecules. *ACS Chem. Biol.* **2019**, *14*, 934–940.

(29) Rurack, K.; Spieles, M. Fluorescence quantum yields of a series of red and near-infrared dyes emitting at 600–1000 nm. *Anal. Chem.* **2011**, *83*, 1232–1242.

(30) Matikonda, S. S.; Hammersley, G.; Kumari, N.; Grabenhorst, L.; Glembockyte, V.; Tinnefeld, P.; Ivanic, J.; Levitus, M.; Schnermann, M. J. Impact of cyanine conformational restraint in the near-infrared range. *J. Org. Chem.* **2020**, *85*, 5907–5915.

(31) Lei, Z.; Li, X.; Luo, X.; He, H.; Zheng, J.; Qian, X.; Yang, Y. Bright, stable, and biocompatible organic fluorophores absorbing/emitting in the deep near-infrared spectral region. *Angew. Chem., Int. Ed.* **2017**, *56*, 2979–2983.

(32) Wang, S.; Fan, Y.; Li, D.; Sun, C.; Lei, Z.; Lu, L.; Wang, T.; Zhang, F. Anti-quenching NIR-II molecular fluorophores for *in vivo* high-contrast imaging and pH sensing. *Nat. Commun.* **2019**, *10*, 1058.

(33) Lei, Z.; Sun, C.; Pei, P.; Wang, S.; Li, D.; Zhang, X.; Zhang, F. Stable, Wavelength-tunable fluorescent dyes in the NIR-II region for *in vivo* high-contrast bioimaging and multiplexed biosensing. *Angew. Chem., Int. Ed.* **2019**, *58*, 8166–8171.

(34) Li, B.; Zhao, M.; Feng, L.; Dou, C.; Ding, S.; Zhou, G.; Lu, L.; Zhang, H.; Chen, F.; Li, X.; et al. Organic NIR-II molecule with long blood half-life for *in vivo* dynamic vascular imaging. *Nat. Commun.* **2020**, *11*, 3102.

(35) Ding, B.; Xiao, Y.; Zhou, H.; Zhang, X.; Qu, C.; Xu, F.; Deng, Z.; Cheng, Z.; Hong, X. Polymethine thiopyrylium fluorophores with absorption beyond 1000 nm for biological imaging in the second near-infrared subwindow. *J. Med. Chem.* **2019**, *62*, 2049–2059.

(36) Lavis, L. D. Chemistry is dead. Long live chemistry! *Biochemistry* **2017**, *56*, 5165–5170.

(37) Bricks, J. L.; Kachkovskii, A. D.; Slominskii, Y. L.; Gerasov, A. O.; Popov, S. V. Molecular Design of near infrared polymethine dyes: a review. *Dyes Pigm.* **2015**, *121*, 238–255.

(38) Streckowski, L. *Heterocyclic Polymethine Dyes: Synthesis, Properties and Applications*; Springer-Verlag: Berlin Heidelberg, 2008.

(39) Stacková, L.; Muchová, E.; Russo, M.; Slavíček, P.; Stacko, P.; Klán, P. Deciphering the Structure-Property Relations in Substituted Heptamethine Cyanines. *J. Org. Chem.* **2020**, *85*, 9776–9790.

(40) Ishchenko, A. A. The length of the polymethine chain and the spectral-luminescent properties of symmetrical cyanine dyes. *Russ. Chem. Bull.* **1994**, *43*, 1161–1174.

(41) Tatikolov, A. S.; Costa, S. M. B. Complexation of polymethine dyes with human serum albumin: a spectroscopic study. *Biophys. Chem.* **2004**, *107*, 33–49.

(42) Li, B.; Lu, L.; Zhao, M.; Lei, Z.; Zhang, F. An efficient 1064 nm NIR-II excitation fluorescent molecular dye for deep-tissue high-

resolution dynamic bioimaging. *Angew. Chem., Int. Ed.* **2018**, *57*, 7483–7487.

(43) Waggoner, A. S.; Mujumdar, R. B. Rigidized trimethine cyanine dyes. Patent US6133445A, October 17, 2000.

(44) Michie, M. S.; Götz, R.; Franke, C.; Bowler, M.; Kumari, N.; Magidson, V.; Levitus, M.; Loncarek, J.; Sauer, M.; Schnermann, M. J. Cyanine conformational restraint in the far-red range. *J. Am. Chem. Soc.* **2017**, *139*, 12406–12409.

(45) Ohulchanskyy, T. Y.; Donnelly, D. J.; Detty, M. R.; Prasad, P. N. Heteroatom substitution induced changes in excited-state photophysics and singlet oxygen generation in chalcogenoxanthylum dyes: effect of sulfur and selenium substitutions. *J. Phys. Chem. B* **2004**, *108*, 8668–8672.

(46) Choi, H. S.; Nasr, K.; Alyabyev, S.; Feith, D.; Lee, J. H.; Kim, S. H.; Ashitate, Y.; Hyun, H.; Patonay, G.; Streckowski, L.; et al. Synthesis and *in vivo* fate of zwitterionic near-infrared fluorophores. *Angew. Chem., Int. Ed.* **2011**, *50*, 6258–6263.

(47) Semonin, O. E.; Johnson, J. C.; Luther, J. M.; Midgett, A. G.; Nozik, A. J.; Beard, M. C. Absolute photoluminescence quantum yields of IR-26 dye, PbS, and PbSe quantum dots. *J. Phys. Chem. Lett.* **2010**, *1*, 2445–2450.

(48) Pengshung, M.; Li, J.; Mukadam, F.; Lopez, S. A.; Sletten, E. M. Photophysical Tuning of Shortwave Infrared Flavylum Heptamethine Dyes via Substituent Placement. *Org. Lett.* **2020**, *22*, 6150–6154.

(49) While many SWIR-emissive donor–acceptor donor dyes have been developed (refs 11, 14–16), broad absorption spectra and low absorption coefficients limit applications within excitation-multiplexed SWIR imaging.

(50) Englman, R.; Jortner, J. The energy gap law for radiationless transitions in large molecules. *Mol. Phys.* **1970**, *18*, 145–164.

(51) Allen, F. H.; Kennard, O.; Watson, D. G.; Brammer, L.; Orpen, A. G.; Taylor, R. Tables of bond lengths determined by X-Ray and neutron diffraction. Part 1. Bond lengths in organic compounds. *J. Chem. Soc., Perkin Trans. 2* **1987**, *12*, S1–S19.

(52) International Commission on Non-Ionizing Radiation Protection. ICNIRP guidelines on limits of exposure to laser radiation of wavelengths between 180 nm and 1,000  $\mu\text{m}$ . *Health Phys.* **2013**, *105*, 271–295.

(53) Philip, R.; Penzkofer, A.; Baumler, W.; Szeimies, R. M.; Abels, C. absorption and fluorescence spectroscopic investigation of indocyanine green. *J. Photochem. Photobiol., A* **1996**, *96*, 137–148.